

INVESTIGATING OPEN CLUSTER KING 6: DETECTION OF THREE NEW VARIABLES

Vaibhav Kumar Pandey,¹ Arvind K. Dattatreya,² Aparna Tripathi,¹ R.K.S Yadav,² Shantanu Rastogi¹

Draft version: April 7, 2025

RESUMEN

ABSTRACT

This study presents photometric analysis of the intermediate-age open cluster King 6, utilizing photometric data in $UBV(RI)_c$ passband and data from the $2MASS$ mission. The Gaia DR3 kinematic data were used to estimate the membership probabilities and $TESS$ data is employed to search for variable stars within the cluster. The cluster's radius is estimated to be $9'.0$ based on the stellar density profile, while optical and near-infrared color-color diagrams revealed color excesses of $E(B - V) = 0.58 \pm 0.03$, $E(J - K) = 0.24 \pm 0.03$, and $E(V - K) = 1.53 \pm 0.01$ mag. Interstellar extinction law is normal in the direction of the cluster. The cluster's estimated age is ~ 251 Myr and distance is 724 ± 5 pc. The mass function slope was found to be $x = 0.57 \pm 0.28$ by considering stars $\geq 1 M_{\odot}$. Our analysis indicates that the cluster is dynamically relaxed. Furthermore, we identified three new variable stars for the first time in the cluster region using $TESS$ data. These variables belong to the category of slow pulsating B-type variables, with periods of 46.70, 47.92, and 37.56 hours.

Key Words: Clusters — photometric — variables — stars

1. GENERAL

Open star clusters serve as fascinating laboratories for exploring our galaxy's stellar evolution and dynamics. They provide insight into star formation processes, enhancing our understanding of the universe (Lada & Lada 2003). Open clusters (OCs) consist of stars with similar physical properties, forming simultaneously from the collapse of a molecular cloud (McKee & Ostriker 2007). While member stars share the same age, distances, and chemical compositions, their masses vary (Joshi et al. 2020a). The study of OCs using astrometric and photometric observations allows us to determine parameters of single star (Dias et al. 2021), partially explaining the interest in these systems. Furthermore, combining astrophysical parameters like distance, metallicity, and age with the kinematic properties of stars within OCs makes them valuable tools for studying formation and evolution of the Galactic disc itself (Cantat-Gaudin et al. 2020). A comprehensive photometric study based on membership determination using proper motions (PMs) and parallaxes helps to understand the stellar and dynamical evolution of the clusters (Tripathi et al. 2023).

King 6 is positioned at ($\alpha_{J2000} = 03:27:55.7$, $\delta_{J2000} = +56:26:38$) corresponding to Galactic coordinates $l \sim 143^{\circ}.36$ and $b \sim -0^{\circ}.07$. Trumpler (1930) classified this cluster as II2m based on

¹Deen Dayal Upadhyaya Gorakhpur University, Gorakhpur, Uttar Pradesh, India, 273009

²Aryabhata Research Institute of Observational Sciences, Manora Peak, Nainital, Uttarakhand, India, 263001

V-band images. Ruprecht (1966) reclassified it in class IV2p. Ann et al. (2002), using $UBVI_c$ CCD photometry, reported mean reddening $E(B - V) = 0.50 \pm 0.10$ mag, $\log(\text{age}) = 8.40 \pm 0.10$ and distance modulus as $(m - M)_0 = 9.70 \pm 0.40$ mag. Maciejewski & Niedzielski (2007) performed a survey in BV wide-field CCD photometry. They estimated core radius as $3'.60 \pm 0'.40$, $\log(\text{age})$ as 8.40, distance modulus as 11.17 ± 0.51 mag, and reddening as 0.53 ± 0.12 mag suggesting no mass segregation within the cluster. Piskunov et al. (2008) found this cluster to be poorly populated. Bossini et al. (2019) catalogued the age and fundamental parameters of 269 open clusters using data from Gaia DR2 and reported $\log(\text{age}) = 8.58 \pm 0.12$, distance modulus 9.54 ± 0.02 , and $A_V = 1.06 \pm 0.03$ for King 6. Gokmen et al. (2023) reported the analysis of King 6 using CCD UBV and Gaia DR3 data. They estimated the colour excess, $E(B - V)$, to be 0.55 ± 0.03 mag and determined the distance as 723 ± 34 pc, with an age of 200 ± 20 Myr. The mass function slope was found to be 1.29 ± 0.18 . Their analysis indicates that the cluster is dynamically relaxed. Table 5 provides a comparative overview of the parameters we derived alongside previously reported values.

There are differences in the parameter values derived for the cluster in the literature, as shown in Table 5. Previous studies on the membership of King 6 did not provide reliable estimates of the cluster members. With the availability of astrometric data from Gaia DR3 and new optical and 2MASS near-infrared data sets, we have revisited the OC King 6 to study their parameters and dynamical status. Additionally, the extracted parameters of the cluster will be used to enhance the sample of clusters needed for studying Galactic structure and dynamics.

The detection of variable stars provides valuable information for constraining stellar pulsation models and refining theoretical models that predict the characteristics of stars in clusters. Pulsating stars, in particular, offer insights into internal stellar structure and mass. Intermediate-age clusters serve as excellent laboratories for studying short-period variables (Joshi et al. 2020b). Recent work on the Pleiades cluster (Bedding et al. 2020) demonstrates the power of combining observations with Gaia (Gaia Collaboration et al. 2016) and *TESS* (Transiting Exoplanet Survey Satellite) for studying pulsating stars in OCs. The large pulsational frequency separation and the frequency at maximum power can help constrain the stellar evolution, structure and oscillation models, leading to a better characterization of pulsating stars. These advancements have encouraged us to use space-based data to characterize the variables in OCs. In this article, we present the results of our search towards variable stars using observational data of the *TESS* mission for King 6 and, in turn, reporting their classification.

The paper is structured as follows: Section 2 presents the observations and data reduction. Section 3 discusses archival data utilized in our analysis. In Section 4, 5, 6, and 7, we have discussed the cluster's parameter. In section 8, we have discussed the luminosity and mass function of the cluster followed by mass segregation, relaxation time and tidal radius in Section 9. Section 10 represents the identification of variable stars in the cluster King 6. Finally, our work is summarized in Section 11.

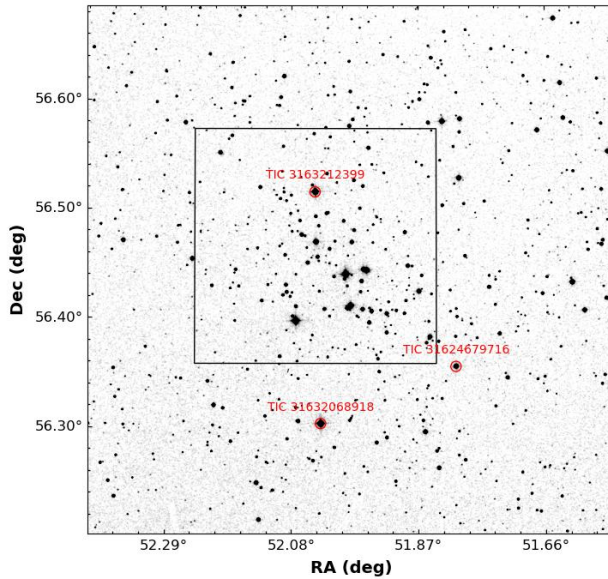


Fig. 1. Identification chart for the cluster King 6, taken from SDSS. Rectangular box outlines observed region, while the red circles highlight position of variable stars.

2. OBSERVATIONS AND DATA REDUCTION

2.1. *UBVRI* photometric observations

This study utilizes data collected with the 104-cm Sampurnanand telescope at the Aryabhata Research Institute of Observational Sciences (ARIES) in Nainital, India. The observations were conducted from December 23rd to 25th, 2005. The telescope captured images in multiple bands: $UBV(IR)_C$, using a thinned, back-illuminated CCD camera mounted at the f/13 Cassegrain focus. Figure 1 presents the finding chart of the cluster, which is taken from the Sloan Digital Sky Survey (SDSS). **The rectangular box indicates the region observed using the 104-cm Sampurnanand telescope at Manora Peak, ARIES, Nainital.**

The CCD detector has pixels measuring $24 \mu\text{m}$ each, arranged in a 2048×2048 grid, providing a field of view on the sky of approximately $13' \times 13'$, with a pixel resolution of $0''.38$. A binning mode of 2×2 pixels was employed during the observations to enhance the signal-to-noise ratio. The CCD have a readout noise of $5.3 e^-$ and a gain factor of $10 e^-/\text{ADU}$. **The Observational log is shown in Table 1.**

For image cleaning, bias and twilight flat-field frames were taken. Multiple short and long exposures were collected for the cluster and standard fields in all filters. Calibrating the stellar magnitudes involved observing stars in the standard field PG1047+003. Several Landolt (1992) standard stars were identified within the observed field of PG1047+003. **The IRAF data re-**

TABLE 1
**DESCRIPTION OF THE OPTICAL OBSERVATION FOR KING 6 AND THE
 STANDARD FIELD**

Cluster/ standard field	Date	Filter	Exp. time × no.of frames
King 6	23/24 th Dec 2005	<i>V</i>	900 × 3, 120 × 1
		<i>B</i>	240 × 2, 1200 × 3
		<i>I</i>	60 × 1, 40 × 1
			100 × 2, 240 × 2
		<i>R</i>	480 × 3, 60 × 1
PG1047+003	25 th Dec 2005	<i>U</i>	300 × 2, 1800 × 2
		<i>V</i>	120 × 4, 100 × 1
		<i>B</i>	200 × 5
		<i>I</i>	60 × 5
		<i>R</i>	60 × 5
	<i>U</i>	300 × 5	

duction package was used for the pre-processing of data frames, which includes bias subtraction, flat fielding, and cosmic ray removal. This process ensures that the data is clean for further analysis.

2.2. Photometric and astrometric calibration

Photometry of bias-subtracted and flat-field corrected CCD frames has been carried out using DAOPHOT-II software (Stetson 1987, 2000). Quantitative values for the brightness of stars are obtained by aperture photometry and profile-fitting photometry. Measurements of bright stars, which are saturated in deep exposure frames, have been taken from short-exposure frames. To translate the observed aperture magnitudes to the standard magnitudes, least-square linear regressions are fitted. The equations for calibrating instrumental magnitudes are as follows:

$$v = V + 4.15 \pm 0.005 - (0.002 \pm 0.004)(B - V) + (0.23 \pm 0.02)X$$

$$b = B + 4.57 \pm 0.008 - (0.005 \pm 0.005)(B - V) + (0.38 \pm 0.02)X$$

$$i = I + 4.62 \pm 0.010 - (0.020 \pm 0.01)(V - I) + (0.10 \pm 0.02)X$$

$$r = R + 4.08 \pm 0.006 - (0.010 \pm 0.004)(V - R) + (0.16 \pm 0.01)X$$

$$u = U + 6.79 \pm 0.030 - (0.006 \pm 0.01)(U - B) + (0.60 \pm 0.08)X$$

Here, V , B , I , R , and U represent standard magnitudes, and v , b , i , r , u refer instrumental aperture magnitudes normalized for 1 sec of exposure time and X is the airmass. The zero points for local standards are evaluated, accounting for the aperture growth curve, difference in exposure times, and atmospheric extinction. The errors associated with the zero points and color coefficients are ~ 0.01 magnitudes.

The internal errors calculated using DAOPHOT are plotted against V magnitudes for the $UBVRI$ filters, as shown in Figure 2. It shows the average photometric error ≤ 0.04 mag across all filters up to a V magnitude of 17 mag. For magnitudes **17 to 20 mag, uncertainty is ~ 0.10 mag whereas for U it is ~ 0.05** . Table 2 analyzes the error trends across filters relative to V magnitude.

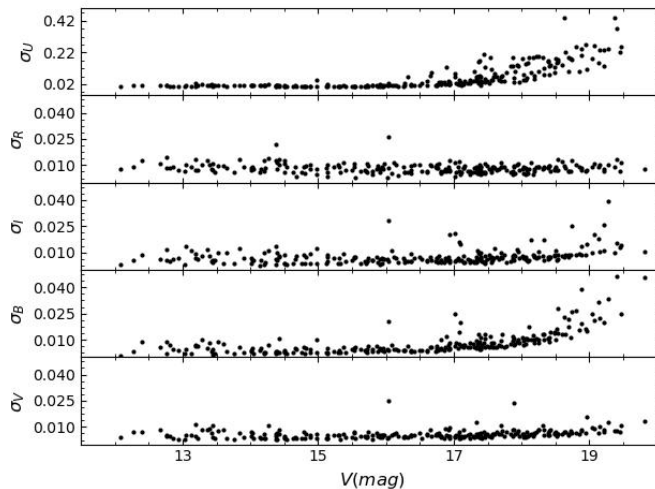


Fig. 2. Photometric errors in V , B , I , R , and U against V -band magnitude. Errors on the Y-axis represent the internal error as estimated by the DAOPHOT routine.

Astrometric solutions are used to get the celestial coordinates of all the stars in $J2000.0$. We use the *CCMAP* and *CCTRAN* tasks of *IRAF* to obtain the celestial coordinates of the detected stars. The sources detected in different wavebands are merged using a matching radius of $\sim 2''$. In total, 3028 stars are detected in all five bands.

2.3. Comparison with the previous photometry

The CCD $UBVI$ photometry was previously done by [Ann et al. \(2002\)](#). To verify our photometry, we have performed the cross-identification of the stars with the photometry by [Ann et al. \(2002\)](#). We have cross-identified 158 stars. We estimated the difference in magnitude and plotted it against V magnitude as shown in Figure 3. The mean of the differences and standard deviation (i.e mean $\pm \sigma$) for V, B, I_c and U magnitude is found to be 0.02 ± 0.09 , 0.01 ± 0.09 , -0.05 ± 0.05 , and 0.04 ± 0.64 mag, respectively.

TABLE 2
DESCRIPTION OF OBSERVED ERRORS IN DIFFERENT FILTERS WITH V MAGNITUDE BINS.

V range	σ_V	σ_B	σ_I	σ_R	σ_U
12-13	0.01	0.01	0.01	0.01	0.01
13-14	0.01	0.01	0.01	0.01	0.02
14-15	0.01	0.01	0.01	0.01	0.02
15-16	0.01	0.01	0.01	0.01	0.04
16-17	0.01	0.02	0.03	0.01	0.10
17-18	0.01	0.03	0.03	0.01	0.20
18-19	0.01	0.04	0.03	0.01	0.40
19-20	0.01	0.10	0.04	0.01	0.50

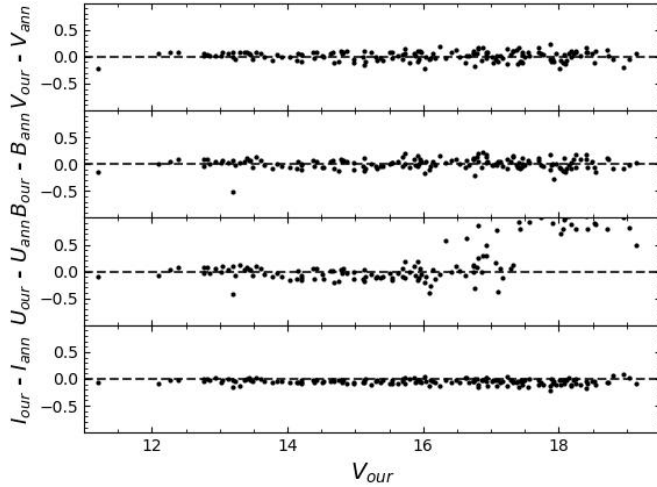


Fig. 3. Comparison of the present photometry with Ann et al. (2002) in U, B, V and I_c filters against V magnitude. The dotted lines are plotted at zero value.

3. ARCHIVAL DATA

3.1. Gaia DR3

The Gaia DR3 data is used for astrometric study and to determine the structural parameters of cluster. It provides celestial positions and G band magnitudes for a vast dataset of approximately 1.8 billion sources, with magnitude measurements extending up to 21 mag. Additionally, Gaia DR3 provides valuable parallax, proper motion, and colour information ($G_{BP} - G_{RP}$) for a subset of

TABLE 3
**DESCRIPTION OF UNCERTAINTIES IN PROPER MOTIONS AND
 MAGNITUDES AGAINST GAIA G MAGNITUDE BINS.**

G(mag)	$\sigma_{\mu_{\alpha} \cos \delta}$	$\sigma_{\mu_{\delta}}$	σ_G	$\sigma_{G_{RP}}$	$\sigma_{G_{BP}}$
11-12	0.020	0.020	0.002	0.003	0.004
12-13	0.020	0.020	0.002	0.003	0.004
13-14	0.030	0.030	0.002	0.004	0.004
14-15	0.040	0.040	0.003	0.005	0.005
15-16	0.050	0.050	0.003	0.006	0.005
16-17	0.070	0.070	0.003	0.010	0.005
17-18	0.114	0.110	0.003	0.030	0.007
18-19	0.198	0.196	0.004	0.070	0.013
19-20	0.384	0.385	0.005	0.120	0.024

this data set, specifically 1.5 billion sources. The uncertainties in parallax values are $\sim 0.02 - 0.03$ milli arcsecond (mas) for sources at $G \leq 15$ mag and ~ 0.07 mas for sources with $G \sim 17$ mag. We have collected data for King 6 within a radius of $30'$. The proper motions of the stars in the cluster and corresponding errors are graphically represented against G magnitude in Figure 4. The lowest panel displays two prominent structures. Uncertainties in the corresponding proper motion components are less than 0.04 mas up to 15^{th} magnitudes; ≤ 0.10 mas from 15^{th} to 18^{th} mag and less than 0.40 mas up to 20^{th} magnitudes. Detailed analysis of uncertainties in proper motion along Right Ascension (RA) and Declination (DEC) and Gaia magnitudes (G , G_{BP} , G_{RP}) is shown in Table 3.

3.2. The Near-infrared Data

We used archival near-infrared photometric data from the Two Micron All-Sky Survey (2MASS) (Skrutskie et al. 2006), which provides photometry in the J ($1.25 \mu\text{m}$), H ($1.65 \mu\text{m}$), and K_s ($2.17 \mu\text{m}$) filters. The data have limiting magnitudes of 15.80, 15.10, and 14.30 in the J , H , and K_s bands, respectively, with a signal-to-noise ratio (S/N) greater than 10. Our optical data were cross-correlated with the 2MASS photometric catalogue, resulting in the identification of 233 common stars within a matching radius of $2''$.

3.3. TESS (Transiting Exoplanet Survey Satellite) data

We have utilized *TESS* data, which features a large plate scale of $21''$ per pixel. This resolution often causes the *TESS* light curves to capture the combined light from multiple stars (Higgins & Bell 2023). In our investigation of the variable stars in our cluster, we identified three isolated stars after matching the *TESS* data with our optical observations.

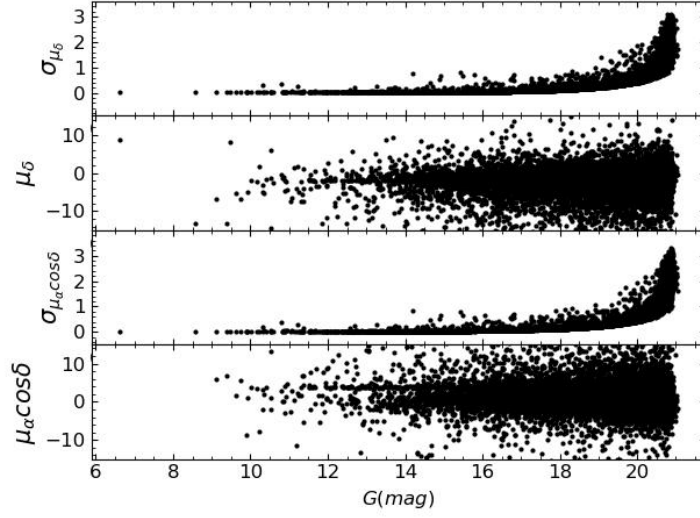


Fig. 4. Proper motions in the direction of RA and DEC and its error are plotted against G mag.

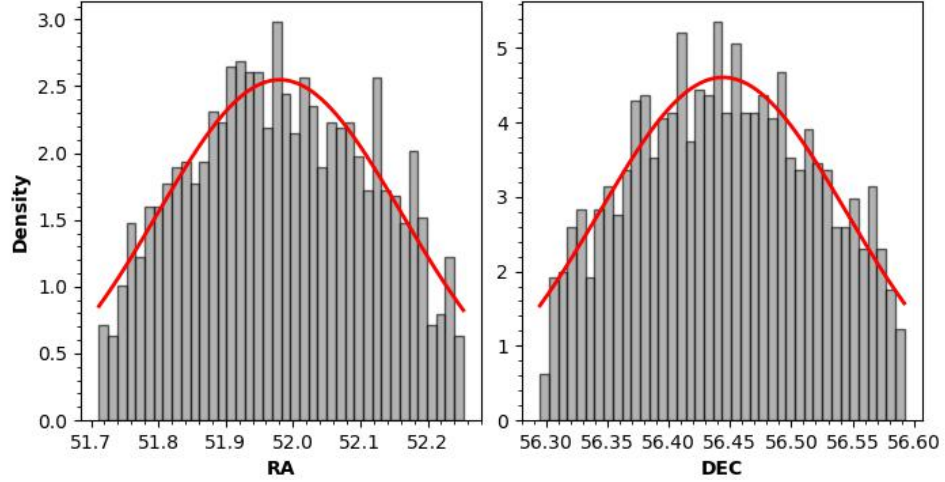


Fig. 5. Histogram in RA and DEC of the stars. Solid red line represents the fitted Gaussian function.

4. STRUCTURAL PARAMETER OF THE CLUSTER: CLUSTER EXTENT

The size of a star cluster plays a crucial role in studying its dynamic evolution, which involves how the cluster changes over time due to internal and external forces. However, determining the precise size of a cluster can be challenging due to its irregular shape, making it difficult to pinpoint

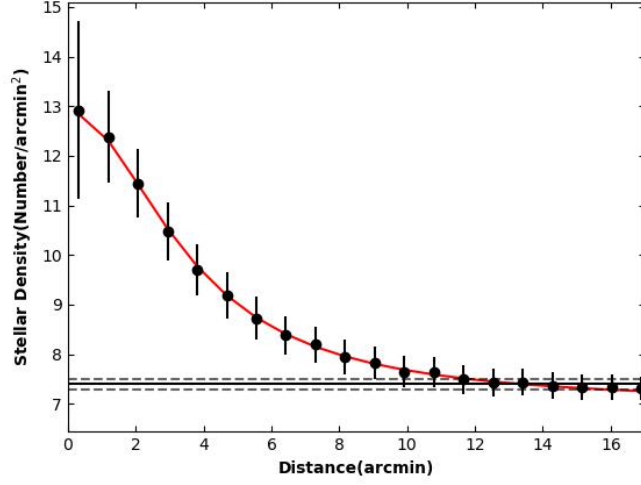


Fig. 6. Radial density profile of the cluster King 6. Red solid curve represents best fit of [King \(1962\)](#). Solid horizontal line represents the background density, whereas dashed lines represent the errors.

the exact centre and outer boundary. To estimate the centre of the cluster, we employed a histogram technique. We plotted the number of stars against their celestial coordinates (RA and DEC) as shown in Figure 5. The data for this analysis comes from Gaia DR3, specifically for stars with a G -band magnitude uncertainty ≤ 0.10 magnitudes and located within a $30'.0$ radius around the cluster centre listed in Table 5. Our analysis reveals cluster centre at approximately (03:27:55.26, +56:26:39.07) for King 6, which is roughly $15''.0$ away from the centre estimated by [Ann et al. \(2002\)](#).

Defining the cluster radius, which indicates the point at which the internal gravitational influence becomes negligible, is a crucial parameter. We achieve this by analyzing the stellar density profile. To conduct a quantitative analysis, we created concentric annular regions (ring-shaped areas) centred on the estimated cluster centre. We then counted the number of stars within each annular ring (width of $0'.50$) and divided this count by the corresponding area of the ring to calculate the number density of stars in that region. This method allows us to examine how the density of stars varies with distance from the cluster center, ultimately helping us determine the effective radius of the cluster. To estimate this radius, we fitted the surface density profile described by [King \(1962\)](#) to the radial distribution of stars. This fit is accomplished using a non-linear least squares routine that takes the error as a weighting factor. The radial density profile (RDP) can be represented as follows:

$$\rho(r) = \frac{\rho_0}{1 + \left(\frac{r}{r_c}\right)^2} + \rho_b \quad (1)$$

where ρ_0 is central density, r_c is core radius of the cluster and ρ_b is the background density.

Figure 6 illustrates the best-fit solution for the density distribution of King 6, along with the associated uncertainties. As evident from the graphs, the radial density profile for the clusters exhibits a decline followed by a flattening behaviour at approximately $9'.0$ for the cluster. Based on this observation, we have adopted $9'.0$ as the cluster radius, which is slightly lower than the values previously reported by Maciejewski & Niedzielski (2007) and Gokmen et al. (2023), as shown in Table 5. For King 6, $\rho_0 = 5.88$ stars/arcmin², $r_c = 3.58$ arcmin and $\rho_b = 7.00$ stars/arcmin². The value of core radius r_c is comparable within error to the values reported by Gokmen et al. (2023) (see Table 5).

5. DETERMINATION OF MEMBERSHIP PROBABILITY

A significant challenge in studying OCs is the presence of unrelated stars along the line of sight, known as field star contamination. Distinguishing these field stars from the cluster's actual members is crucial for accurately estimating the cluster's physical and dynamical properties (Angelo et al. 2019, 2020). An effective method for separating members from field stars is the vector point diagram (VPD) based on proper motions (Dias et al. 2018). The unprecedented astrometric precision of the Gaia DR3 catalogue has significantly improved the reliability of membership determination based on kinematic data (data related to stellar motion) (Castro-Ginard et al. 2018; Castro-Ginard et al. 2019); (Liu & Pang 2019). Therefore, we used data from Gaia DR3 for our kinematic analysis, member star identification, and cluster distance calculations. Figure 7 illustrates the VPDs constructed using the proper motion of stars in RA and Dec for the cluster. Here, the cluster stars are separated from the field stars, with the cluster members encircled in red as shown in the upper panel of the figure, and the cluster members are separated from the field stars shown by CMD in the lower panel of Figure 7. This distinction is possible because cluster stars exhibit a more concentrated distribution in their proper motions than field stars. The centre of the red circle is determined using the maximum density method used by Joshi et al. (2020a).

The estimated value of the centre of cluster proper motion distribution is found to be $(\mu_\alpha \cos \delta, \mu_\delta) = 3.82$ mas yr⁻¹, -1.90 mas yr⁻¹ for King 6. We identified stars within the red circle as probable member stars. We found a total of 575 probable member stars for the cluster. To quantify the membership of stars, we calculated the membership probabilities. We estimated membership probabilities using a statistical approach based on PMs of stars as described in previous studies (Sanders (1971); Michalska (2019); Pandey et al. (2020)).

Assuming a distance of 0.75 kpc and a radial velocity dispersion of 1 km s⁻¹ for open clusters (Girard et al. 1989), a dispersion (σ_c) of ~ 0.28 mas yr⁻¹ in the proper motion of the cluster can be obtained. We calculated $\mu_{xf} = 0.15$ mas yr⁻¹, $\mu_{yf} = -0.74$ mas yr⁻¹, $\sigma_{xf} = 5.76$ mas yr⁻¹, and $\sigma_{yf} = 5.53$ mas yr⁻¹ for the field stars. These values are used to construct the frequency distributions of the cluster stars (ϕ_c^ν) and the field stars (ϕ_f^ν) using the equation given in Yadav et al. (2013). The value of the membership probability for the i^{th} star is calculated using the equation given below:

$$P_\mu(i) = \frac{n_c \times \phi_c^\nu(i)}{n_c \times \phi_c^\nu(i) + n_f \times \phi_f^\nu(i)} \quad (2)$$

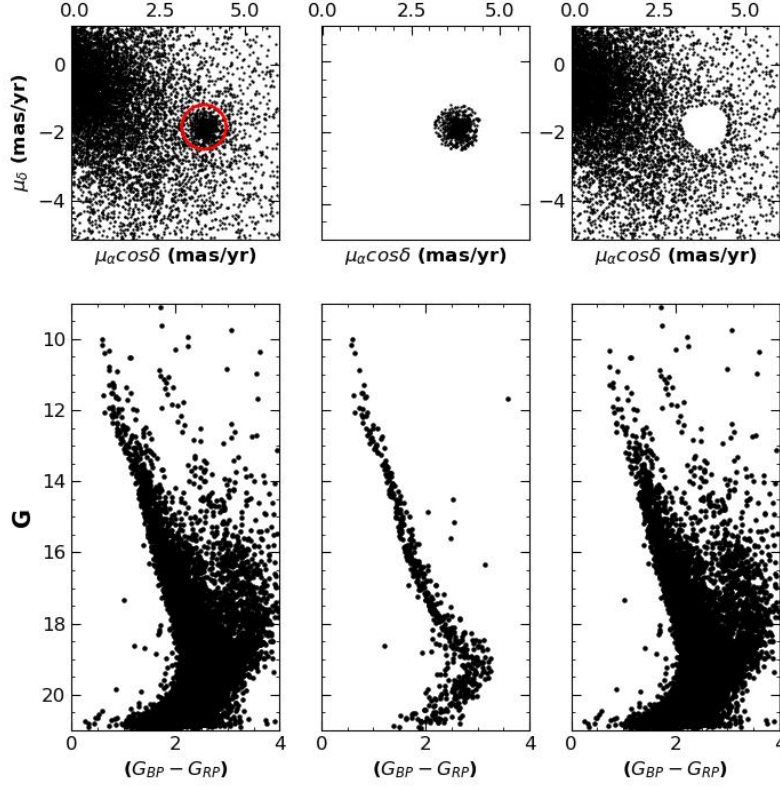


Fig. 7. Initial cluster member separation using proper motion. Top panels show the VPDs and bottom panels show the respective CMDs for total, cluster and field region.

where n_c and n_f are the normalized numbers of probable cluster members and field stars, respectively. We have found 606 stars with $P_\mu > 0.80$ for the cluster. In Figure 8, we have plotted the membership probability against G magnitude. In this figure, we can see the separation between cluster members and field stars toward brighter part, which supports the effectiveness of this technique. A high membership probability extends to $G \sim 20$ mag, whereas the probability gradually decreases toward the fainter limits. We matched our $UBVRI$ catalogue with the Gaia catalogue using a matching radius of $2''.0$. We found 242 optical counterparts of Gaia sources with membership probability information. We found 94 stars within the cluster radius ($9'$) having membership probability $P_\mu \geq 0.80$.

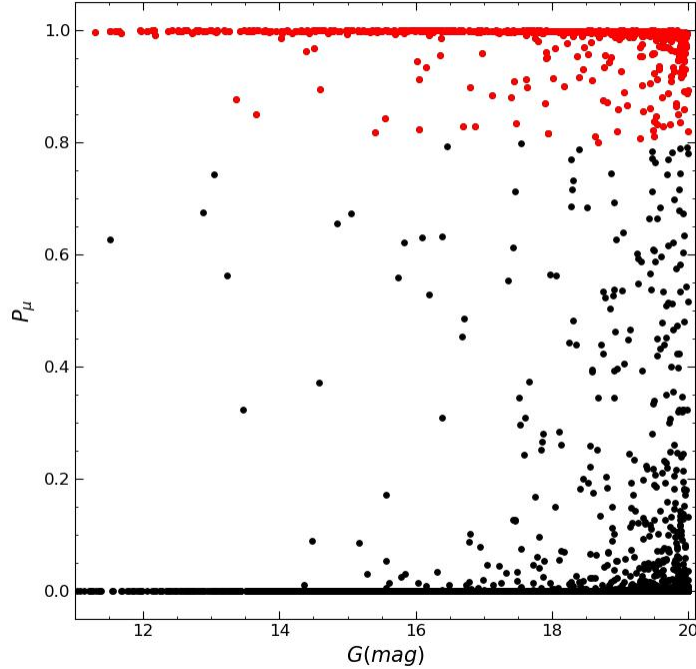


Fig. 8. The Gaia membership probability is plotted against G magnitude. The red dot represents the star with a probability of $P_\mu \geq 0.80$, and the black dots represent the star with a probability of $P_\mu < 0.80$.

6. CLUSTER PARAMETERS

6.1. $(U - B)$ vs $(B - V)$ diagram

The reddening, $E(B - V)$, can be determined by fitting intrinsic zero-age main-sequence (ZAMS) on the $(U - B)/(B - V)$ colour-colour diagram (Phelps & Janes 1994). **The black points denote member stars present within a $9'.0$ radius and with probability $P_\mu > 0.80$.** The best fit of the intrinsic ZAMS was achieved by shifting $E(B - V)$ along the reddening vector as shown in Figure 9. We adopted the slope of the reddening vector $E(U - B)/E(B - V) = 0.72$ and fitted the ZAMS with the solar metallicity, i.e., $Z = 0.02$ (Schmidt-Kaler et al. 1982). The best fit was achieved for the reddening value of 0.58 ± 0.03 mag. Our estimated value of $E(B - V) = 0.58 \pm 0.03$ mag is comparable to the values estimated by Maciejewski & Niedzielski (2007), Gokmen et al. (2023), and Ann et al. (2002) (see Table 5).

6.2. Total-to selective extinction value

Reddening is an important parameter for a star cluster since it can significantly affect the determination of other fundamental parameters. Colour-colour diagrams are essential for understanding

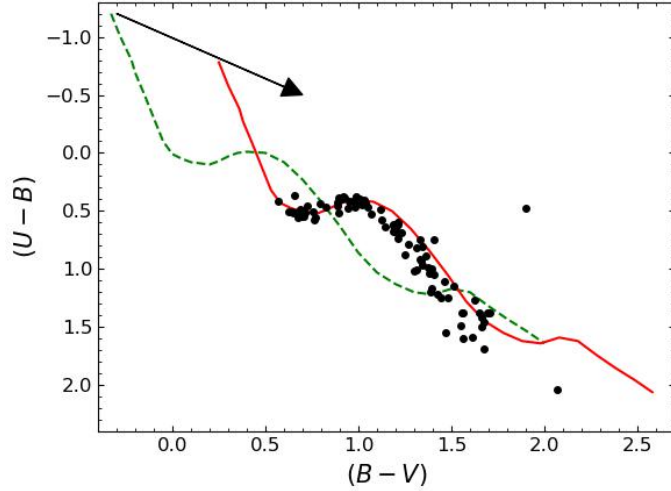


Fig. 9. The colour-colour diagram for target region. Dashed line represents intrinsic ZAMS, while the solid curve represents best-fit ZAMS line. Arrow illustrates the reddening vector.

the extinction law. The emitted photons of cluster stars are scattered and absorbed in the interstellar medium by dust particles, which leads to the deviation of colours from their intrinsic values. The normal Galactic reddening law may not accurately describe the reddening observed along the line of sight to many star clusters (Snedden et al. 1978). To examine the nature of the reddening law, two colour diagrams, $(V - \lambda)/(B - V)$, are employed as suggested by Chini & Wargau (1990), where λ represents all filters other than V . Here, we have examined the reddening law for the cluster by drawing two colour diagrams, as shown in Figure 10. Since the stellar colour values emerge to show the linear relationship, a linear equation is applied to calculate the slope ($m_{cluster}$). We have calculated the total-to-selective extinction using the relation given by Neckel & Chini (1981):

$$R_{cluster} = \frac{m_{cluster}}{m_{normal}} \times R_{normal} \quad (3)$$

where R_{normal} is the normal value of total-to-selective extinction taken to be 3.10, and m_{normal} and $m_{cluster}$ are the slopes of a linear fit to two colour diagrams for normal extinction and extinction in the direction of clusters, respectively. The values of m_{normal} and $m_{cluster}$ are given in Table 4. The average $R_{cluster}$ ($=2.78 \pm 0.30$) is approximately equal to the normal value. Thus, the reddening law is normal in the direction of the cluster.

6.3. Distance and Age Determination

A CMD has been used to estimate the cluster's age and distance. V versus $(U - B)$, V versus $(B - V)$, and V versus $(V - I)$ CMDs of the member stars (represented by blue dots) within the cluster radius $9'.0$ and the $P_{\mu} \geq 0.80$ are shown in Fig 11. The CMDs of the target cluster show a

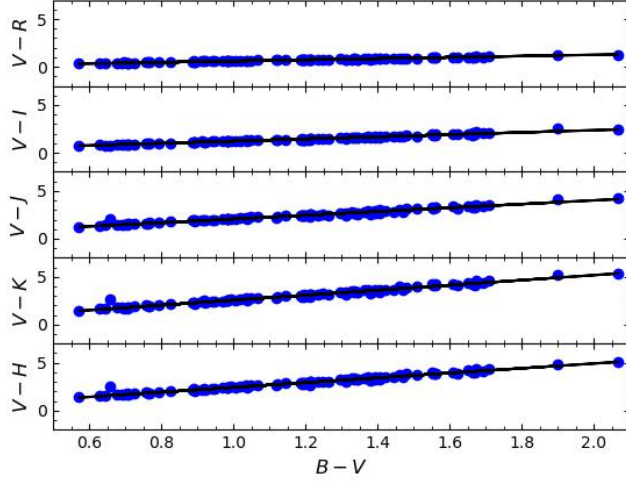


Fig. 10. $(V - \lambda)/(B - V)$ colour-colour diagram is plotted for stars within cluster radius, with membership probability $P_\mu > 0.80$. Continuous line represents the slopes.

TABLE 4

THE SLOPES OF THE $(V - \lambda)/(B - V)$ DIAGRAMS FOR THE MEMBER STARS AND CORRESPONDING NORMAL VALUES.

	$\frac{(V-R)}{(B-V)}$	$\frac{(V-I)}{(B-V)}$	$\frac{(V-J)}{(B-V)}$	$\frac{(V-K)}{(B-V)}$	$\frac{(V-H)}{(B-V)}$
Normal	0.80	1.70	2.23	2.72	2.42
King 6	0.66 ± 0.001	1.34 ± 0.001	1.94 ± 0.001	2.61 ± 0.001	2.49 ± 0.001
$R_{cluster}$	2.56	2.44	2.70	2.97	3.19

well-defined narrow main sequence (MS). MS extends from $V \sim 11.2 - 18.8$ mag. The theoretical isochrone of solar metallicity $Z = 0.02$ taken from Bertelli et al. (1994) have been overplotted on the CMDs and represented by solid lines. The reddening values derived in Section 6.1 were used for the isochrone fitting. The best fit of the theoretical isochrone gives the value of distance modulus as $(V - M_v) = 11.10 \pm 0.40$ mag, giving the distance to be 724 ± 5 pc. Our estimated distance value is comparable with the values derived by Maciejewski & Niedzielski (2007) and Gokmen et al. (2023) (see Table 5).

We have also used parallax of the stars to obtain the distance of the cluster. In Figure 12, we plotted the histogram of 0.10 mas parallax bin using the star within the cluster radius with the probability membership $P_\mu \geq 0.80$. A Gaussian function is fitted on the histogram. We found a mean parallax of 1.36 ± 0.10 mas. Using this mean parallax, we estimated the distance as 735 ± 10 pc, which closely agrees with the value derived using CMDs.

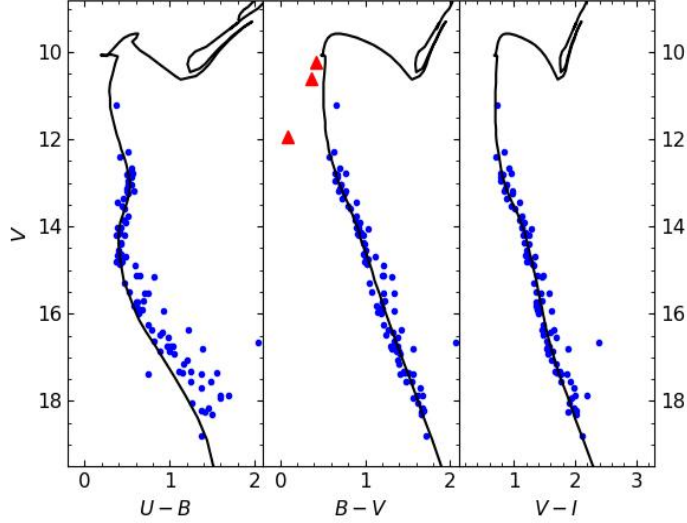


Fig. 11. The colour-magnitude diagrams for the member stars of the cluster with $P_\mu \geq 0.80$. The red triangles represent positions of variable stars using data from [Stassun et al. \(2019\)](#).

The age of the cluster has been determined by fitting theoretical stellar evolutionary isochrones of different ages on the CMDs ($V/(U - B)$, $V/(B - V)$, and $V/(V - I)$). The isochrone fitting is done considering the bluest envelope of the CMDs, as shown in Figure 11. After correcting for reddening, the best fit is obtained for an age of $\log(\text{age}) = 8.40$ (~ 251 Myr), which is in good agreement with the previously estimated values by [Ann et al. \(2002\)](#); [Gokmen et al. \(2023\)](#) and [Maciejewski & Niedzielski \(2007\)](#), listed in Table 5.

7. INTERSTELLAR EXTINCTION IN NEAR-IR

7.1. $(V - K)$, $(J - K)$ diagram

We have combined *2MASS* JHK_s data with the optical data to determine interstellar extinction in near-IR. The K_s magnitude is converted into K magnitude using the methods given by [Persson et al. \(1998\)](#). The $(J - K)$ versus $(V - K)$ colour-colour diagram for the cluster members is shown in the left panel of Figure 13. The solid line in the figure shows the ZAMS given by [Bertelli et al. \(1994\)](#). This ZAMS provides $E(J - K) = 0.24 \pm 0.03$ mag and $E(V - K) = 1.50 \pm 0.01$ mag for the cluster. The ratio $\frac{E(J-K)}{E(V-K)}$ is $\sim 0.16 \pm 0.03$, which is in good agreement with the normal interstellar extinction value 0.19 given by [Cardelli et al. \(1989\)](#). This scatter is due to the large error in the JHK data.

7.2. $(B - V)$ vs $(J - K)$ diagram

We have plotted $(B - V)$ versus $(J - K)$ colour-colour diagram for the cluster, as shown in the middle panel of the Fig 13. We have used the ZAMS given by [Bertelli et al. \(1994\)](#) to know the

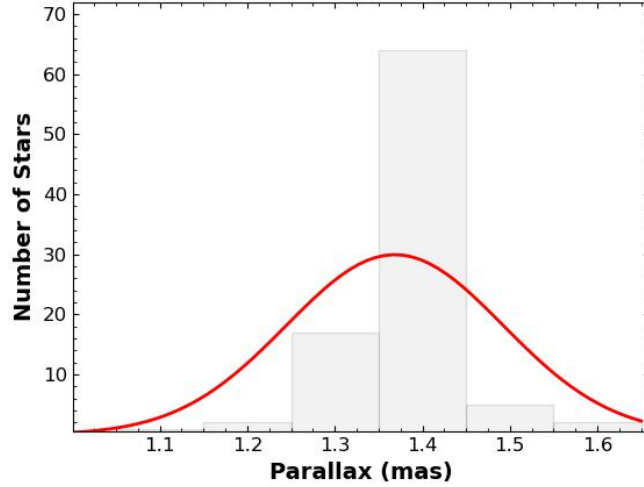


Fig. 12. Histogram in parallax (0.10 mas bins) for the cluster region. Red curve represents the Gaussian function fitting.

relationship between these two colours. The colour excess $E(B - V)$ and $E(J - K)$ is found to be 0.58 and 0.24 mag. This results in a ratio of $\frac{E(B-V)}{E(J-K)} \sim 0.43$ mag, which is slightly lower than the value of 0.56 reported in the literature (Cardelli et al. 1989).

7.3. $(J - H)$ vs $(J - K)$ diagram

The $(J - H)$ vs $(J - K)$ colour-colour diagram for the cluster is shown in the right panel of Figure 13. To determine the relation between these two colours we have utilized ZAMS given by Bertelli et al. (1994) as indicated by the solid line in the right panel of the figure. We have found that $E(J - H) = 0.15 \pm 0.02$ and $E(J - K) = 0.24 \pm 0.03$. We have calculated the value of the ratio $\frac{E(J-H)}{E(J-K)} = 0.64 \pm 0.06$ which is in agreement within 2σ the normal value 0.55 as quoted by Cardelli et al. (1989).

7.4. Age and distance of the cluster using 2MASS data

Using 2MASS data, we re-determined the distance and age of the cluster. We have plotted V versus $(V - K)$ in the left panel, J versus $(J - H)$ in the middle panel, and K versus $(J - K)$ in the right panel in Figure 14. We have used the theoretical isochrone given by Bertelli et al. (1994) for $Z = 0.02$ of $\log(\text{age}) = 8.40$, which has been overplotted in the CMDs. We have found the apparent distance modulus of 11.10 ± 0.08 , 9.82 ± 0.08 , and 9.57 ± 0.08 mag using the CMDs respectively shown in Figure 14. This distance modulus leads to a distance of 733 ± 7 pc. The age and the distance of the cluster derived using 2MASS data agree with those derived using optical data.

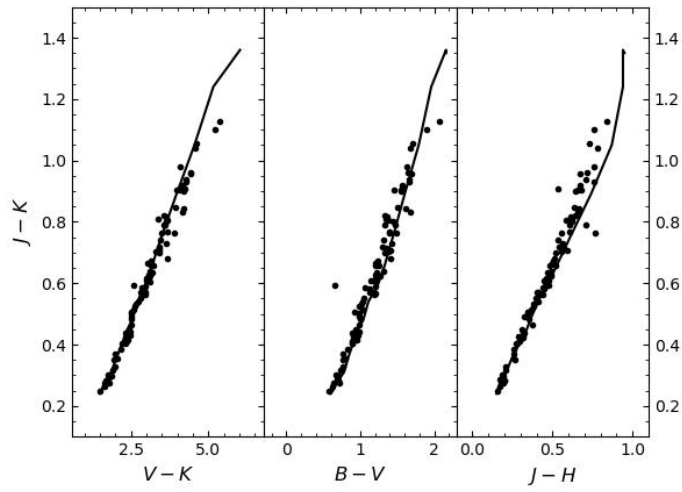


Fig. 13. Colour-colour diagram for the stars within the cluster radius and $P_\mu \geq 0.8$. Solid line is the ZAMS taken from Bertelli et al. (1994).

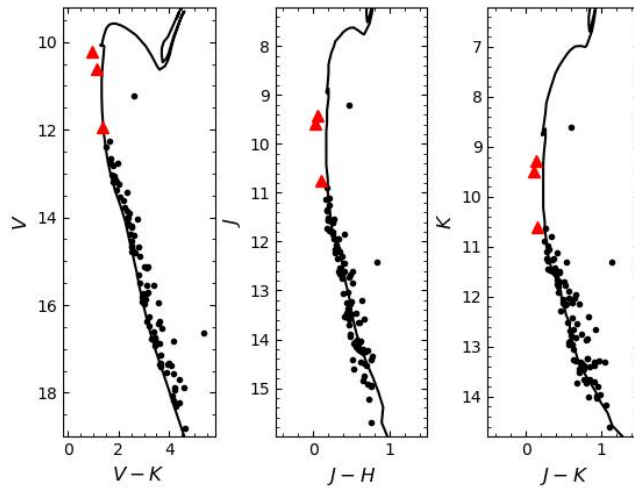


Fig. 14. Colour-magnitude diagram for the stars within cluster radius and $P_\mu \geq 0.80$. Triangular red dots represent the position of variable stars.

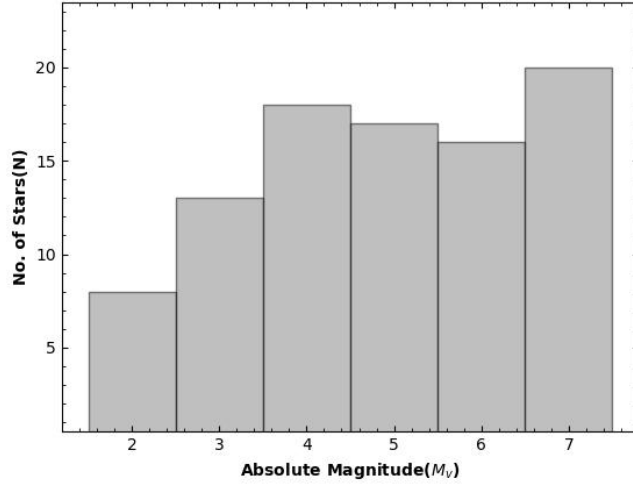


Fig. 15. Luminosity function of the cluster region.

8. LUMINOSITY AND MASS FUNCTION

8.1. Luminosity Function

We examined the brightness distribution of stars within the cluster. To achieve this, we considered the stars with the probability $P_\mu \geq 0.80$ and within the cluster radius. We considered their apparent brightness (V magnitude) and converted it to their true brightness (absolute magnitude) by accounting for the cluster's distance and a correction factor (A_V). We grouped stars in brightness (bins of 1.00 magnitude) to ensure enough stars in each group for reliable analysis. Finally, by plotting the number of stars in each brightness bin, we created a luminosity function(LF) for the cluster, shown in Figure 15. Interestingly, this distribution shows an increasing trend up to $M_v \sim 4$ mag and a dip at ~ 5.50 mag for the cluster.

8.2. Mass Function

The mass function (MF), i.e., the frequency distribution of stellar masses, is a fundamental parameter in studying star formation and evolution in the cluster. It represents the distribution of stellar masses per unit volume in a star formation event, and knowledge of MF is very effective in determining the subsequent evolution of the cluster. The MF can be derived using the linear relation :

$$\log(dN/dM) = -(1 + x) \times \log M + \text{constant} \quad (4)$$

where dN represents the number of stars per mass bin dM with the central mass M , and x is the slope of the MF. To convert the LF to the MF, we used the theoretical evolutionary model given by Bertelli et al. (1994), and the resulting MF is shown in Figure 16. This figure shows a turn ~ 1

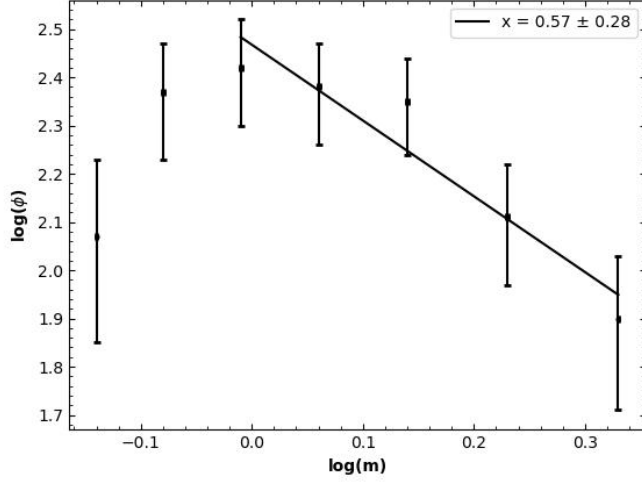


Fig. 16. Mass Function for cluster under study derived using Bertelli et al. (1994) isochrone. The error bars represent $\frac{1}{\sqrt{N}}$

M_{\odot} . To derive the mass function slope, we consider the stars to have a mass $\geq 1 M_{\odot}$. The derived slope of the MF is $x = 0.57 \pm 0.28$, which is less than the value 1.35 given by Salpeter (1955) for Solar neighbourhood stars. The calculated mass function slope is less than the mass function slope 1.29 ± 0.18 determined by Gokmen et al. (2023) within the mass range $0.58 \geq M/M_{\odot} \geq 3.59$.

9. MASS SEGREGATION, RELAXATION TIME AND TIDAL RADIUS OF THE CLUSTER

9.1. Mass segregation

To study the mass segregation of the cluster, we plotted the cumulative radial distribution of the stars for different masses as shown in Figure 17. To do so, we have divided the main sequence stars in the two mass ranges, $3.10 \leq M/M_{\odot} \leq 1.25$ and $1.25 \leq M/M_{\odot} \leq 0.68$ for the cluster. To obtain the mass segregation effect, we have selected the probable member based on the membership probability and CMD of the cluster. The figure exhibits the mass segregation effect in the sense that massive stars gradually sink towards the cluster centre rather than the fainter star. To check whether this mass distribution represents the same kind of distribution, we have performed the Kolmogorov-Smirnov(K-S) test. This test indicates that the confidence level of the mass segregation effect is 98 % for the cluster.

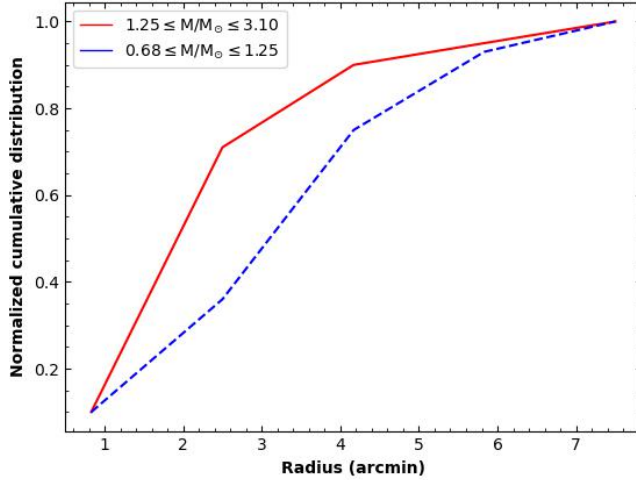


Fig. 17. The cumulative radial distribution of member stars in low-mass ($< 1.25M_{\odot}$) and relatively higher-mass ($\geq 1.25M_{\odot}$) range .

9.2. The relaxation time

The relaxation time (T_E) is the time scale in which the cluster loses all traces of its initial condition. It is the peculiar time scale for the cluster to reach some extent of energy equipartition. The relaxation time is given by [Spitzer Jr & Hart \(1971\)](#):

$$T_E = \frac{8.9 \times 10^5 (NR_h^3)^{1/2}}{\langle m \rangle^{1/2} \log(0.4N)} \quad (5)$$

where N is the number of cluster members with probability ($P_{\mu} \geq 0.80$) and within radius $9'.00$, R_h is the half-mass radius of the cluster and $\langle m \rangle$ is the mean mass of the cluster stars ([Spitzer Jr & Hart 1971](#)). In our case, the value of $\langle m \rangle$ is found to be $1 M_{\odot}$. The value of the R_h is assumed to be the half of the radius derived by us in Section 4. Using the above relation, we estimated the cluster's dynamical relaxation time T_E to be 6.0 Myr. A comparison of the cluster's relaxation time with the cluster's age indicates that the relaxation time is smaller than the cluster's age. Therefore, we conclude that the cluster is dynamically relaxed.

9.3. Tidal radius

The tidal radius of the cluster is the extent to which the gravitational influence of the Galaxy is equal to that of the gravitational influence caused by the cluster core. It can be determined using the following procedure.

The Galactic Mass M_G inside a Galactocentric Radius R_G is given by (Genzel & Townes 1987)

$$M_G = 2 \times 10^8 M_\odot \left(\frac{R_G}{30 \text{ pc}} \right)^{1.2} \quad (6)$$

The value of M_G is found to be $1.83 \times 10^{11} M_\odot$. Using the formula by Kim et al. (2000), the tidal radius of the cluster can be obtained as

$$R_t = \left(\frac{M_c}{2M_G} \right)^{1/3} \times R_G \quad (7)$$

where R_t and M_c are the cluster's tidal radius and total mass, respectively. The mass of the cluster is calculated by considering the overall mass function slope derived in this article within the mass range $0.68\text{-}3.10 M_\odot$. Thus, the derived tidal radius of the cluster is found to be 3.18 pc. **A comparative analysis of the fundamental parameters of King 6, as derived in this study and reported in the literature, is presented in Table 5.**

10. VARIABLE STARS IN THE CLUSTER KING 6

The variable stars are the objects that change their brightness over time. This variation provides critical insight into the physical processes governing stars. In the present study, we used the *TESS* data to search the variable stars in the cluster region. We found three variable stars (TIC 31624679716, TIC 31632068918, and TIC 3163212399) that were isolated in the SDSS image. These variables are plotted in the CMDs shown in Figure 11 and Figure 14. We have used the light curve provided by *TESS* to analyse these variables. The periodicity of these variables is determined using the Lomb-scargle algorithm provided by Scargle (1982), Lomb (1976) for unevenly spaced light curves. The effective temperature (T_{eff}) taken from SIMBAD is 11055, 10510, and 10510 K for TIC 31624679716, TIC 31632068918, and TIC 3163212399 stars, respectively. The value of temperature suggests that they are B-type stars. The light curves of each variable are analysed below.

10.1. TIC 31624679716

The light curve of the star TIC 31624679716 ($RA = 51.8077 \text{ deg}$, $DEC = 56.3553 \text{ deg}$) is shown in Figure 18. The upper panel shows the light curve, while the middle panel shows the phase folded light curve. The light curve shows a coherent periodic variability in the star. The change in magnitude in the light curve is ~ 0.02 mag. The lower panel shows the Lomb-Scargle periodogram computed from the data shown in the upper panel. The detected period of the variable star is found to be 46.70 hrs.

10.2. TIC 31632068918

Figure 19 shows the light curve of the variable star TIC 31632068918 ($RA = 52.0315 \text{ deg}$, $DEC = 56.3031 \text{ deg}$). The upper and middle panels display the light curve and phase folded light curve, while the lower panel shows the Lomb-Scargle periodogram computed from the data shown in the upper panel. The variation in magnitude is estimated to be ~ 0.01 mag. The derived period of this variable star is 47.92 hrs.

TABLE 5
**COMPARISON OF OUR DERIVED FUNDAMENTAL PARAMETERS OF KING
 6 WITH THE LITERATURE VALUES**

Parameters	Numerical Values	Reference
(RA, DEC) (deg)	$(51.98 \pm 0.18, 56.44 \pm 0.10)$	Present study
	51.98, 56.44	(Ann et al. 2002)
$(\mu_\alpha \cos \delta, \mu_\delta)$ (mas yr ⁻¹)	$(-3.82, -1.90)$	Present study
Cluster Radius (arcmin)	9'.00	Present study
	10'.90	(Maciejewski & Niedzielski 2007)
	10'.00	(Gokmen et al. 2023)
Cluster Radius(pc)	1.98	Present study
Tidal Radius(pc)	3.18	Present study
ρ_0 (stars/arcmin ²)	5.88 ± 0.87	Present study
	2.28 ± 0.24	(Gokmen et al. 2023)
r_c (arcmin)	3.58 ± 0.49	Present study
	4.68 ± 1.07	(Gokmen et al. 2023)
ρ_b (stars/arcmin ²)	7.00 ± 0.06	Present study
	5.12 ± 0.16	(Gokmen et al. 2023)
log(age)	8.40	Present study
	8.40 ± 0.10	(Ann et al. 2002)
	8.40	(Maciejewski & Niedzielski 2007)
	8.58 ± 0.12	(Bossini et al. 2019)
	8.29	(Dias et al. 2021)
	8.30	(Gokmen et al. 2023)
Distance (pc)	724 ± 5	Present study
	426	(Ann et al. 2002)
	800 ± 270	Maciejewski & Niedzielski (2007)
	497	(Bossini et al. 2019)
	704	(Dias et al. 2021)
	723 ± 34	(Gokmen et al. 2023)
$E(B - V)$ (mag)	0.58 ± 0.03	Present study
	0.50 ± 0.10	(Ann et al. 2002)
	0.53 ± 0.12	(Maciejewski & Niedzielski 2007)
	0.34	(Bossini et al. 2019)
	0.59	(Dias et al. 2021)
	0.55 ± 0.03	(Gokmen et al. 2023)
$E(J - K)$ (mag)	0.24 ± 0.03	Present study
$E(V - K)$ (mag)	1.50 ± 0.01	Present study
$R_{cluster}$	2.78 ± 0.30	Present study
A_v	1.80	Present study
	1.596 ± 0.09	(Gokmen et al. 2023)
Mass function slope (x)	0.57 ± 0.28	Present study
Relaxation Time(Myrs)	6.0	Present study

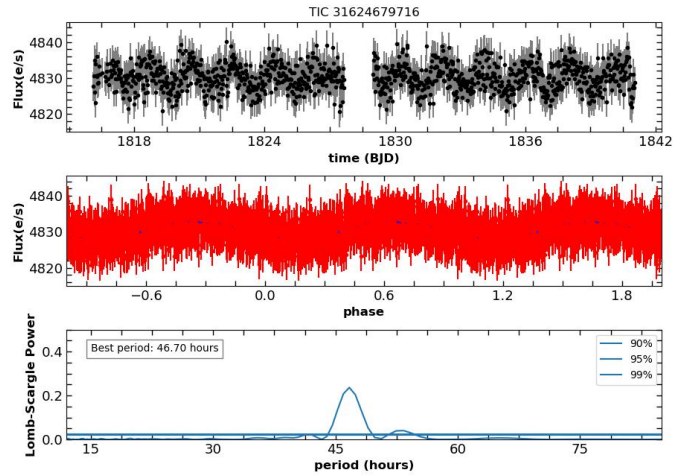


Fig. 18. Light curves for the star TIC 31624679716. Upper panel shows light curve, while middle and lower panels show phase-folded light curve and the periodogram.

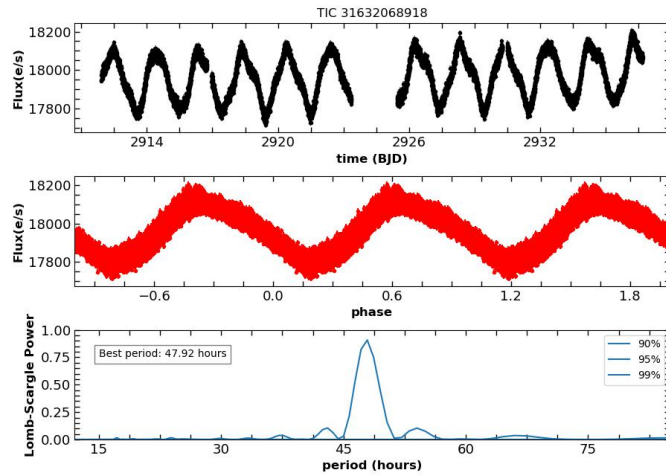


Fig. 19. Same as Figure 18 for the variable star TIC 31632068918.

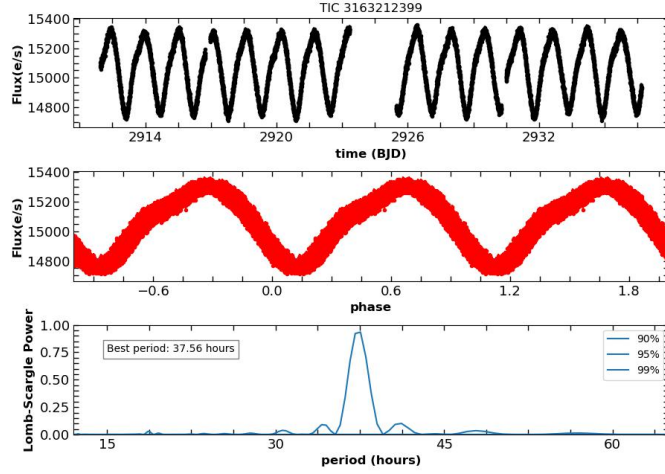


Fig. 20. Same as Figure 18 for the variable star TIC 3163212399.

10.3. TIC 3163212399

The *TESS* light curve of the variable star TIC 3163212399 ($RA = 52.0408deg$, $DEC = 56.5152deg$) is shown in Figure 20. The upper, middle and lower panels display the light curve, phase folded light curve and Lomb-Scargle periodogram. A coherent periodicity is observed in the light curve, indicating a magnitude variation of ~ 0.04 mag for the star. The determined period of the star is 37.56 hours.

10.4. H-R Diagram and classification of the variables

The variable stars can be classified using the location of the stars on the H-R diagram, the shape of their light curve, variability amplitude, and periods. The variable stars searched in this study are plotted in the H-R diagram depicted in Figure 21. The dotted line is the main-sequence curve taken from Pecaut & Mamajek (2013), and the black curve is the region for the slow pulsating B-type (SPB) stars (Miglio et al. 2007). Our study has identified three variables near the SPB region. The period ranges from 0.30 to 5 days for SPB-type stars, and the magnitude variation should be generally less than 0.10 mag. We classify these stars as SPB variables based on their location in the H-R diagram, period, spectral type, magnitude variation, and light curve shape.

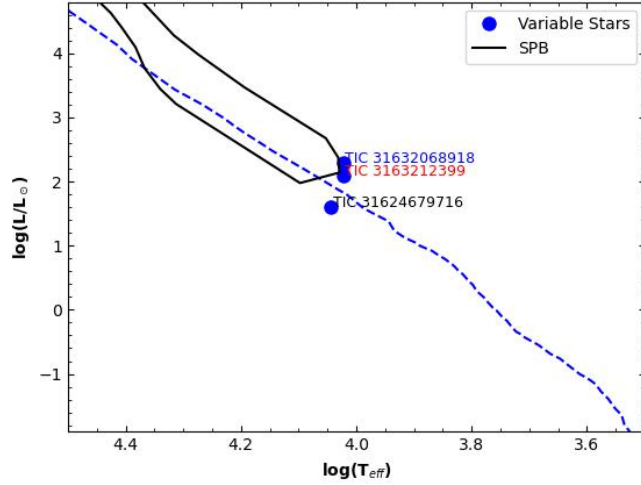


Fig. 21. Hertzsprung-Russell ($\log(L/L_{\odot})$ vs. $\log(T_{eff})$) diagram for periodic variables within the cluster region.

11. CONCLUSION

We have studied the intermediate age open star cluster King 6 using $UBV(RI)_c$, $2MASS JHK$, $GAIADR3$ and $TESS$ data. The main findings of our analysis are as follows:

1. The cluster radius is found to be $9'.0$, which corresponds to 1.98 pc at the cluster's distance. The tidal radius of the cluster is determined to be 3.18 pc.
2. From the colour-colour diagram, we have estimated $E(B - V) = 0.58 \pm 0.03$ for the cluster. The JHK data, in combination with the optical data, provide $E(J - K) = 0.24 \pm 0.03$ while $E(V - K) = 1.50 \pm 0.01$. The value of R_v is found to be 2.78 ± 0.30 . Hence, our analysis indicates that the interstellar extinction law is normal in the direction of the cluster.
3. The age of the cluster is found to be 251 Myrs, which is determined using the theoretical isochrone of Bertelli et al. (1994) of solar metallicity $Z = 0.02$.
4. The distance of the cluster is estimated to be 724 ± 5 pc. The distance value is supported by the values determined using near-IR data and parallax.
5. The luminosity function is determined by considering probable members. We found an increasing trend up to $M_v \sim 4.0$ mag and a dip at ~ 5.50 mag for the cluster. The overall mass function slope is 0.57 ± 0.28 , which is less than the Salpeter (1955) value.
6. There is clear evidence of mass segregation within the cluster. The Kolmogorov-Smirnov test indicates a 98% confidence level for this mass segregation. Additionally, the relaxation time of the cluster is determined as 6.0 Myr, suggesting that the cluster is dynamically relaxed.

7. We searched variable stars in the cluster region finding three variables with *TESS* ID *TIC* 31624679716, *TIC* 31632068918, and *TIC* 3163212399 for the first time. The variation in magnitude of the variable stars is 0.02, 0.01, and 0.04 mag, and the period is 46.70, 47.92, and 37.56 hrs, respectively classifying them as Slow Pulsating B-type stars.

12. ACKNOWLEDGEMENT

We are thankful to the anonymous referee for their constructive suggestion on this paper which has improved it a lot. We also acknowledge the use of data from the European Space Agency (ESA) mission Gaia (processed by the Gaia Data Processing and Analysis Consortium, DPAC), which is publicly available from the Gaia Data Release 3 (DR3) and the use of data products from the Two-Micron All Sky Survey (*2MASS*), a joint project of the University of Massachusetts and the Infrared Processing and Analysis Center/California Institute of Technology, funded by NASA and the National Science Foundation. This work has made use of data obtained from the Transiting Exoplanet Survey Satellite (*TESS*) mission, which is funded by NASA Science Mission Directorate. Furthermore, we are grateful to the Aryabhata Research Institute of Observational Sciences (ARIES) for its support and contribution to this research.

REFERENCES

- Angelo, M., Piatti, A. E., Dias, W. S., et al. 2019, *MNRAS*, 488, 1635
 Angelo, M., Santos Jr, J., & Corradi, W. 2020, *MNRAS*, 493, 3473
 Ann, H. B., Lee, S. H., Sung, H., et al. 2002, *ApJ*, 123, 905 [\[LINK\]](#)
 Bedding, T. R., Murphy, S. J., Hey, D. R., et al. 2020, *Nature*, 581, 147
 Bertelli, G., Bressan, A., Chiosi, C., et al. 1994, *A&AS*, 106, 275
 Bossini, D., Vallenari, A., Bragaglia, A., et al. 2019, *A&A*, 623, A108 [\[ADS\]](#)
 Cantat-Gaudin, T., Anders, F., Castro-Ginard, A., et al. 2020, *A&A*, 640, A1
 Cardelli, J. A., Clayton, G. C., & Mathis, J. S. 1989, *ApJ*, 345, 245 [\[ADS\]](#)
 Castro-Ginard, A., Jordi, C., Luri, X., et al. 2018, *A&A*, 618, A59 [\[ADS\]](#)
 Castro-Ginard, A., Jordi, C., Luri, X., et al. 2019, *A&A*, 627, A35
 Chini, R. & Wargau, W. F. 1990, *A&A*, 227, 213 [\[ADS\]](#)
 Dias, W., Monteiro, H., & Assafin, M. 2018, *MNRAS*, 478, 5184
 Dias, W. S., Monteiro, H., Moitinho, A., et al. 2021, *MNRAS*, 504, 356
 Gaia Collaboration, Brown, A. G. A., Vallenari, A., et al. 2016, *A&A*, 595, A2 [\[ADS\]](#)
 Genzel, R. & Townes, C. 1987, *ARA&A*, 25, 377
 Girard, T. M., Grundy, et al. 1989, *ApJ*, 98, 227
 Gokmen, S., Eker, Z., Yontan, T., et al. 2023, *ApJ*, 166, 263
 Higgins, M. E. & Bell, K. J. 2023, *ApJ*, 165, 141
 Joshi, Y. C., John, A. A., Maurya, J., et al. 2020b, *MNRAS*, 499, 618 [\[ADS\]](#)
 Joshi, Y. C., Maurya, J., John, A. A., et al. 2020a, *MNRAS*, 492, 3602
 Kim, S. S., Figer, D. F., Lee, H. M., et al. 2000, *ApJ*, 545, 301 [\[LINK\]](#)
 King, I. 1962, *ApJ*, 67, 471
 Lada, C. J. & Lada, E. A. 2003, *ARA&A*, 41, 57 [\[LINK\]](#)
 Landolt, A. U. 1992, *ApJ*, 104, 340
 Liu, L. & Pang, X. 2019, *ApJS*, 245, 32

- Lomb, N. R. 1976, *Astrophys. Space Sci.*, 39, 447
- Maciejewski, G. & Niedzielski, A. 2007, *A&A*, 467, 1065
- McKee, C. F. & Ostriker, E. C. 2007, *ARA&A*, 45, 565
- Michalska, G. 2019, *MNRAS*, 487, 3505
- Miglio, A., Montalbán, J., & Dupret, M.-A. 2007, *MNRASL*, 375, L21
- Neckel, T. & Chini, R. 1981, *A&AS*, 45, 451 [\[ADS\]](#)
- Pandey, R., Sharma, S., Panwar, N., et al. 2020, *ApJ*, 891, 81
- Pecaut, M. J. & Mamajek, E. E. 2013, *ApJS*, 208, 9
- Persson, S. E., Murphy, D. C., Krzeminski, W., et al. 1998, *ApJ*, 116, 2475 [\[LINK\]](#)
- Phelps, R. L. & Janes, K. A. 1994, *ApJS*, 90, 31
- Piskunov, A., Schilbach, E., Kharchenko, N., et al. 2008, *A&A*, 477, 165
- Ruprecht, J. 1966, *Bull. Astron. Inst. Czechosl.*, 17, 98 [\[ADS\]](#)
- Salpeter, E. E. 1955, *ApJ*, 121, 161
- Sanders, W. 1971, *A&A*, 14, 226
- Scargle, J. D. 1982, *ApJ*, 263, 835 [\[ADS\]](#)
- Schmidt-Kaler, T. et al. 1982, *Stars and Star Clusters*, 1st edn., Vol. 2d (Springer-Verlag), 14–24 [\[LINK\]](#)
- Skrutskie, M., Cutri, R., Stiening, R., et al. 2006, *ApJ*, 131, 1163
- Snedden, C., Gehrz, R. D., Hackwell, J. A., et al. 1978, *ApJ*, 223, 168 [\[ADS\]](#)
- Spitzer Jr, L. & Hart, M. H. 1971, *ApJ*, 166, 483
- Stassun, K. G., Oelkers, R. J., Paegert, M., et al. 2019, *AJ*, 158, 138 [\[ADS\]](#)
- Stetson, P. B. 1987, *Publ. Astron. Soc. Pac*, 99, 191 [\[LINK\]](#)
- . 2000, *Publ. Astron. Soc. Pac*, 112, 925 [\[LINK\]](#)
- Tripathi, A., Panwar, N., Sharma, S., et al. 2023, *JAA*, 44, 61
- Trumpler, R. J. 1930, *Lick Observatory Bulletin*, 420, 154 [\[ADS\]](#)
- Yadav, R. K. S., Sariya, D. P., & Sagar, R. 2013, *MNRAS*, 430, 3350 [\[LINK\]](#)

Full addresses go here